6

Sensorless First- and Second-Order Sliding-Mode Control of a Wind Turbine-Driven Doubly-Fed Induction Generator

Ana Susperregui, Gerardo Tapia and M. Itsaso Martinez
University of the Basque Country (UPV/EHU)
Spain

1. Introduction

The doubly-fed induction generator (DFIG) is a wound-rotor electric machine on which about 75% of the wind turbines installed nowadays are based. As sketched in Fig. 1, when generating power, its stator is directly connected to the grid, while a back-to-back double-bridge converter —comprising both the rotor- (RSC) and grid-side (GSC) converters— interfaces its rotor with the grid, hence allowing the flow of slip power both from the grid to the rotor —at subsynchronous speeds— and vice-versa —at supersynchronous speeds— within a certain speed range.

Given that only the slip power has to be managed by the bidirectional rotor converter, it is sufficient to size it so that it typically supports between 25% and 30% of the DFIG rated power (Ekanayake et al., 2003; Peña et al., 1996). This is more than probably the main reason for the success of the DFIG in the field of variable-speed wind generation systems.

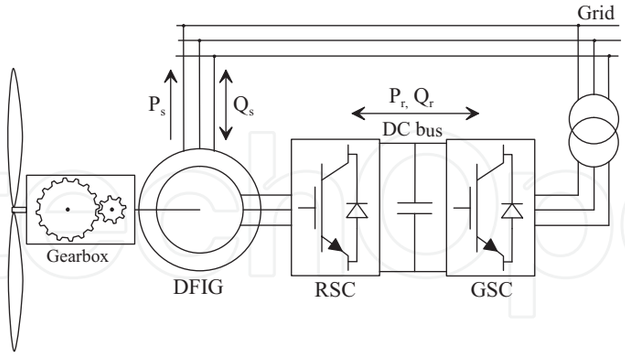

Fig. 1. Structure of a DFIG-based wind turbine

Standard field oriented control (FOC) schemes devised to command wind turbine-driven DFIGs comprise proportional-integral (PI)-controlled cascaded current and power loops, which require the use of an incremental encoder (Tapia et al., 2003). Although stator-side active and reactive powers can be independently governed by adopting those control schemes, the system transient performance degrades as the actual values of the DFIG resistances and inductances deviate from those based on which the control system tuning was carried out during commissioning (Xu & Cartwright, 2006). In addition, the optimum

power curve tracking achievable using PI-based control schemes shows a considerable room for improvement. Even if feedforward decoupling control terms are traditionally incorporated to enhance the closed-loop DFIG dynamic response, they are extremely dependent on DFIG parameters (Tapia et al., 2006; Xu & Cartwright, 2006).

In this framework, alternative high dynamic performance power control schemes for DFIGs are being proposed, among of which a strong research line focuses on the so-called direct power control (DPC) (Xu & Cartwright, 2006; Zhi & Xu, 2007). Several others explore the alternative of applying sliding-mode control (SMC), both standard —first-order— (Beltran et al., 2008; Susperregui et al., 2010), and higher-order (Beltran, Ahmed-Ali & Benbouzid, 2009; Beltran, Benbouzid & Ahmed-Ali, 2009; Ben Elghali et al., 2008).

Moreover, since, as already mentioned, the back-to-back rotor converter is sized to manage a slip power up to 25% or 30% of the wind generator rated power, DFIGs are kept connected to the grid provided that their rotational speed remains within a certain range. Accordingly, connection of DFIGs to the grid is only accomplished if the wind is strong enough to extract energy from it profitably. In particular, the four-pole 660-kW DFIG considered in this chapter is not connected to the grid until its rotational speed exceeds the threshold value of 1270 rpm. Yet, connecting the DFIG stator to the grid is not straightforward. In fact, although wind-turbine-driven DFIGs are asynchronous machines, owing to the double-bridge rotor converter managing the slip power, they behave as real synchronous generators. Accordingly, prior to connecting the stator of a DFIG to the grid, the voltage induced at its stator terminals must necessarily be synchronized to that of the grid.

However, even though control of wind turbine-driven DFIGs is a topic extensively covered in the literature, not many contributions outline or describe in some detail possible strategies for smooth connection of DFIGs to the grid. So far, the synchronization problem has been approached from different viewpoints, hence giving rise to alternative methods, as open-loop stator voltage control (Peña et al., 2008), closed-loop regulation of rotor current (Peresada et al., 2004; Tapia et al., 2009), and phase-locked loop (PLL) (Abo-Khalil et al., 2006; Blaabjerg et al., 2006) or even direct torque control (DTC) of the voltage induced at the open stator (Arnaltes & Rodríguez, 2002).

Considering those precedents, together with the robustness and tracking ability naturally conferred by SMC, both a first-order and a higher-order sensorless SMC algorithms, conceived to command the RSC feeding the rotor of a DFIG, are described and evaluated in this chapter. Those two algorithms are not only aimed at governing active and reactive power exchange between the DFIG stator and the grid, but also at ensuring the synchronization required for smooth connection of the DFIG stator to the grid.

The chapter is organized as follows. Given that the DFIG exhibits different dynamics depending on whether its stator is connected to the grid or not (Tapia et al., 2009), the mathematical model corresponding to each of those two operating conditions is first briefly presented. Conditions to reach synchronization are also provided. After selection of the switching functions associated, respectively, to the power control and synchronization objectives, a global first-order sliding-mode control (1-SMC) algorithm, based on Utkin's research work on various other types of electric machines (Utkin et al., 1999; Utkin, 1993; Yan et al., 2000), is described in detail. Stability analyses are also provided for both the power control and synchronization operation regimes. An overall second-order sliding-mode control (2-SMC) algorithm, alternative to the previous one, is next presented. Special attention is paid to the derivation of effective tuning equations for all its gains and constants. The practical issue related to bumpless transition between the controllers in charge of synchronization

and power control, at the instant of connecting the DFIG stator to the grid, is then tackled. Adaptation of the model reference adaptive system (MRAS) observer put forward in (Peña et al., 2008), so that it remains valid for sensorless control during synchronization, is also dealt with. Sensorless versions of the two SMC algorithms proposed are evaluated via real-time hardware-in-the-loop (HIL) emulation over a virtual 660-kW DFIG prototype. The chapter finishes with a conclusion section, devoted to analyze the results arising from the HIL emulation tests carried out.

2. Review of DFIG model and grid synchronization

Focused on a 660-kW DFIG, the main objective of the two alternative versions of the control system presented along this chapter consists in succeeding in the achievement of the maximum active power the machine is able to generate at each rotational speed; i.e., to track the DFIG optimum power curve. As a secondary goal, but still essential from the point of view of the electricity supply quality, the reactive power the machine generates or absorbs from the grid is also managed.

Before raising the modelling of the machine, and, to get ride of misunderstandings due to the diverse nomenclature used to identify the reference frames taking part in FOC, Fig. 2 presents the terminology that is going to be adopted hereafter. It can be observed that the stator direct and quadrature axes are represented as sD and sQ, respectively, and that the rotor reference frame, which forms the θ_r turning angle with respect to sD axis, is denominated $r\alpha$-$r\beta$. Since the machine is going to be rotor-side controlled, the magnitudes will be referred to a frame, labeled as x-y, whose direct axis is aligned with the stator flux, $\vec{\psi}_s$ —and, therefore, with the stator magnetizing current, $\vec{i}_{ms}$. The latter reference frame is turned ρ_s with respect to the sD-sQ plane.

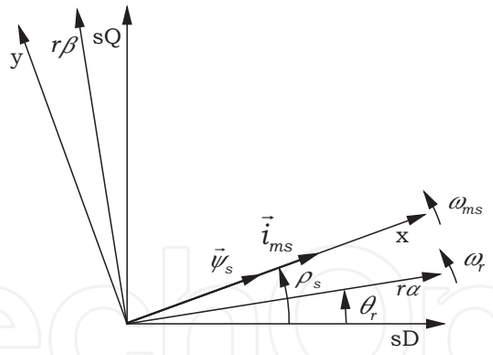

Fig. 2. Stator-flux-oriented reference frame

When connected to the grid, the rotor-side-voltage generator model regarding the stator-flux-oriented reference frame —x-y— may be expressed as (Tapia et al., 2009; Vas, 1998)

$$v_{rx} = R_r i_{rx} + L'_r \frac{di_{rx}}{dt} + \frac{L_m}{L_s} \frac{d|\vec{\psi}_s|}{dt} - \omega_{sl} L'_r i_{ry} \tag{1}$$

$$v_{ry} = R_r i_{ry} + L'_r \frac{di_{ry}}{dt} + \omega_{sl} \frac{L_m}{L_s} |\vec{\psi}_s| + \omega_{sl} L'_r i_{rx}, \tag{2}$$

where v_{rx} and v_{ry} are the components of the rotor voltage, i_{rx} and i_{ry} represent the rotor currents, and $\omega_{sl} = \omega_{ms} - \omega_r$ stands for the slip frequency between the $r\alpha$ and x axes. R_r, L_s

and L_m denote the rotor resistance, and the stator and magnetizing inductances, respectively. Finally, $L'_r = \sigma L_r$ symbolizes the transient inductance of the rotor, where $\sigma = 1 - L_m^2/(L_s L_r)$ is the total leakage factor.

Taking into account that power generation is not profitable at low speeds —less than 1270 rpm in this particular case—, the generator will not be connected to the grid until this threshold value is exceeded. Therefore, a new "grid-non-connected" state appears where the machine dynamic behaviour differs from that in which its stator is connected to the grid, and, consequently, the model changes. Moreover, the transition between the disconnected and connected states is not trivial, since the grid voltage and that induced at the open stator of the DFIG may present magnitude and/or phase differences. At this point, aiming at removing the risk of short circuit, it can be taken advantage of a properly controlled "grid-non-connected" state, turning it into a synchronization stage.

Let a new x'-y' reference frame be defined when the stator is disconnected from the grid, where, as shown in Fig. 3, its y' quadrature axis and the grid voltage space-phasor are collinear. Moreover, assuming steady-state regime, and, if rotor current is stable, it can be demonstrated (Tapia et al., 2009) that the stator flux and voltage space-vectors are collinear to x and y axes, respectively; i.e., $\vec{\psi}_s \perp \vec{v}_s$.

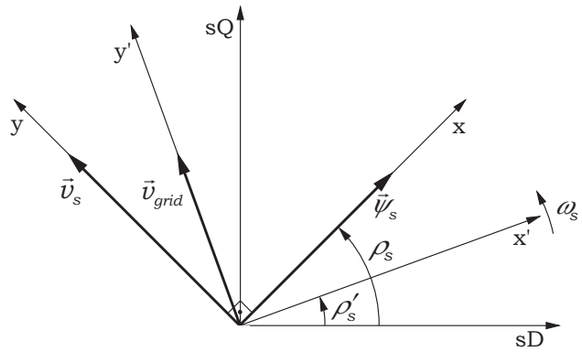

Fig. 3. New reference frame for synchronization

Bearing in mind that stator current is null when disconnected from the grid, the new open-stator model, expressed according to the x'-y' reference frame, arises (Tapia et al., 2009):

$$v_{rx'} = R_r i_{rx'} + L_r \frac{di_{rx'}}{dt} - \omega_{sl} L_r i_{ry'} \rightarrow \frac{di_{rx'}}{dt} = \frac{v_{rx'}}{L_r} - \frac{R_r}{L_r} i_{rx'} + \omega_{sl} i_{ry'} \tag{3}$$

$$v_{ry'} = R_r i_{ry'} + L_r \frac{di_{ry'}}{dt} + \omega_{sl} L_r i_{rx'} \rightarrow \frac{di_{ry'}}{dt} = \frac{v_{ry'}}{L_r} - \frac{R_r}{L_r} i_{ry'} - \omega_{sl} i_{rx'}. \tag{4}$$

As evidenced in Fig. 3, synchronization may be achieved if x-y and x'-y' reference frames are aligned. However, for a complete match-up, the grid and stator voltage space-vectors must be not only collinear but also identical in magnitude. The two conditions are satisfied if the following rotor current values are achieved (Tapia et al., 2009):

$$i_{rx'ref} = \frac{\left|\vec{v}_{grid}\right|}{\omega_s L_m};\ i_{ry'ref} = 0, \tag{5}$$

and, consequently, synchronization is ensured; i.e.:

$$i_{rx} = i_{rx'} = \frac{\left|\vec{v}_{grid}\right|}{\omega_s L_m};\ i_{ry} = i_{ry'} = 0;\ \rho_s = \rho'_s. \tag{6}$$

Furthermore, if the current values presented in (6) are substituted into the stator-side reactive and active power expressions given next (Vas, 1998):

$$Q_s = \frac{3}{2}\frac{|\vec{v}_s|}{L_s}(|\vec{\psi}_s| - L_m i_{rx});\ P_s = -\frac{3}{2}\frac{L_m}{L_s}|\vec{v}_s| i_{ry}, \tag{7}$$

it follows that, at the instant of the connection, zero power-exchange is achieved.
For the sake of a proper performance of the whole system, each state must be commanded with its own controller. Moreover, the transition between the two states must carefully be followed up, depending on the control strategy being applied, in order to achieve a bumpless connection. This aspect will be thoroughly described in a later section.

3. Sensorless sliding-mode control arrangement for the DFIG

Aiming to track the optimum power curve of the DFIG, sliding-mode control theory has been adopted, which provides the system with superior tracking ability and high robustness despite uncertainties or parameter variations. The basis of SMC is the judicious election of a switching variable, which usually depends on a linear combination of the error of the variable to be commanded and its subsequent time derivatives. Here, the proposed switching variables for optimum power control —stator connected to the grid— are

$$s_{Q_s} = e_{Q_s} + c_Q \int e_{Q_s} dt \tag{8}$$

$$s_{P_s} = e_{P_s} + c_P \int e_{P_s} dt, \tag{9}$$

where $e_{Q_s} = Q_{s\,ref} - Q_s$ and $e_{P_s} = P_{s\,ref} - P_s$ represent de errors in reactive and active powers, respectively, and the integral terms, weighted by c_Q and c_P positive constants, are added for steady-state response improvement (Utkin et al., 1999).
Examining the set-points proposed in (5), it can be derived that rotor current regulation must be carried out if synchronization is required. Therefore, when the stator is disconnected from the grid, and, similarly to the previous case, the following switching functions are suggested:

$$s_{i_{rx'}} = e_{i_{rx'}} + c_{x'} \int e_{i_{rx'}} dt \tag{10}$$

$$s_{i_{ry'}} = e_{i_{ry'}} + c_{y'} \int e_{i_{ry'}} dt, \tag{11}$$

where $e_{i_{rx'}} = i_{rx'\,ref} - i_{rx'}$ and $e_{i_{ry'}} = i_{ry'\,ref} - i_{ry'}$ represent the errors in $i_{rx'}$ and $i_{ry'}$, respectively, and $c_{rx'}$ and $c_{ry'}$ are positive constants.
The switching variable defines the relative degree of a system, and, as a result, the order of the applicable SMC (Levant, 1993). As the system is of first-order relative degree in both states, connected and disconnected from the grid, it may be commanded applying 1-SMC or 2-SMC (Bartolini et al., 1999). The design of the two controllers is detailed in subsequent sections.

3.1 First-order sliding-mode control

In this section, a 1-SMC scheme is proposed. Due to the different dynamic behaviours presented by the DFIG when disconnected or connected to the grid, a different DFIG model is considered to conceive the control of each of those two cases, and a first-order sliding-mode controller is accordingly synthesized for each of them.

In particular, the 1-SMC applied is that based on V. I. Utkin's research work (Utkin et al., 1999; Utkin, 1993; Yan et al., 2000), which sets out the following: most of the electrical systems must modulate the control signals in order to command the transistors' gates of their converters; so, why not directly generate those gating signals thus eluding the use of pulse-width modulation (PWM) or space-vector modulation (SVM) techniques? (Yan et al., 2008) This theory fits perfectly the present case, in which controllers for the RSC of the back-to-back configuration are designed for the two possible connection states of the DFIG.

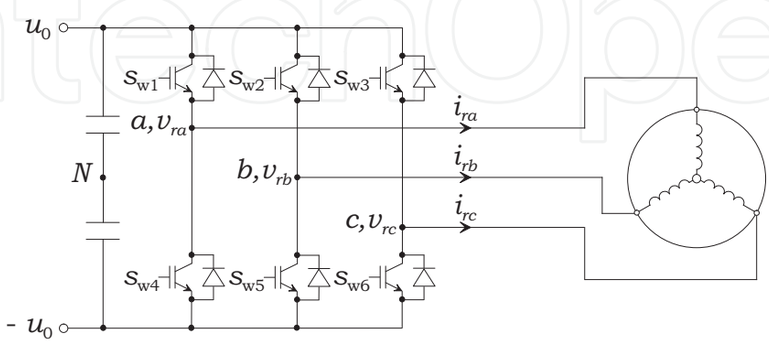

Fig. 4. Rotor-side converter scheme

Depending on whether or not the DFIG stator is connected to the grid, its model and controllers do vary, but the RSC to be commanded, displayed in Fig. 4, remains obviously the same. Analyzing this scheme (Utkin et al., 1999), it is possible to find a link between:

- the signals generated by controllers based on a synchronous frame, v_{rx} and v_{ry}, and those between the midpoints of the converter legs and the DC link, v_{raN}, v_{rbN} and v_{rcN}:

$$\overbrace{\begin{bmatrix} v_{rx} \\ v_{ry} \end{bmatrix}}^{\mathbf{V}_{xy}} = \overbrace{\begin{bmatrix} \cos\rho & \cos(\rho - \frac{2\pi}{3}) & \cos(\rho + \frac{2\pi}{3}) \\ -\sin\rho & -\sin(\rho - \frac{2\pi}{3}) & -\sin(\rho + \frac{2\pi}{3}) \end{bmatrix}}^{\mathbf{D}} \overbrace{\begin{bmatrix} v_{raN} \\ v_{rbN} \\ v_{rcN} \end{bmatrix}}^{\mathbf{V}_{abc}} . \tag{12}$$

  If the opposite relation is needed, the inverse of **D** matrix must exist. But, as it is not square, Moore-Penrose pseudo-inverse concept (Utkin et al., 1999) may be used to calculate its inverse, $\mathbf{D}^{+} = \mathbf{D}^{T}(\mathbf{D}\mathbf{D}^{T})^{-1}$, resulting the previous matrix expression in:

$$\begin{bmatrix} v_{raN} \\ v_{rbN} \\ v_{rcN} \end{bmatrix} = \overbrace{\begin{bmatrix} \cos\rho & -\sin\rho \\ \cos(\rho - \frac{2\pi}{3}) & -\sin(\rho - \frac{2\pi}{3}) \\ \cos(\rho + \frac{2\pi}{3}) & -\sin(\rho + \frac{2\pi}{3}) \end{bmatrix}}^{\mathbf{D}^{+}} \begin{bmatrix} v_{rx} \\ v_{ry} \end{bmatrix}, \tag{13}$$

  where $\rho = \rho_s - \theta_r$.

- the voltages v_{raN}, v_{rbN} and v_{rcN}, and the transistors' gating signals, s_{w1}, s_{w2}, s_{w3}, s_{w4}, s_{w5} and s_{w6}:

$$\begin{array}{ll} s_{w1} = 0.5(1 + v_{raN}/u_0) & s_{w4} = 1 - s_{w1} \\ s_{w2} = 0.5(1 + v_{rbN}/u_0) & s_{w5} = 1 - s_{w2} \\ s_{w3} = 0.5(1 + v_{rcN}/u_0) & s_{w6} = 1 - s_{w3} \end{array} . \tag{14}$$

The following sections describe the design of the control scheme for the cases mentioned above: DFIG connected to and disconnected from the grid.

3.1.1 DFIG connected to the grid —Optimum power generation

Once synchronization is completed and the DFIG is connected to the grid, it is going to be commanded applying the following multivariable control law, in order to achieve optimum power generation:

$$\mathbf{V}_{abc} = -u_0 \mathrm{sgn}(\mathbf{S}), \tag{15}$$

where $\mathbf{S} = \begin{bmatrix} s_1 & s_2 & s_3 \end{bmatrix}^T$ contains the switching variable expressions represented in *a-b-c* three-phase reference frame. Note that, as the system to be controlled presents negative gain, that of the control law must also be negative if stability is pursued.

Aiming to ease the design of the controllers and, subsequently, to demonstrate the stability of the closed-loop system, the model can be transferred to subspace $\mathbf{S}_{QP} = \begin{bmatrix} s_{Q_s} & s_{P_s} \end{bmatrix}^T$, if the time derivatives of (8) and (9) are taken, and making use of (1)-(2):

$$\overbrace{\begin{bmatrix} \dot{s}_{Q_s} \\ \dot{s}_{P_s} \end{bmatrix}}^{\dot{\mathbf{S}}_{QP}} = \overbrace{\begin{bmatrix} F_1 \\ F_2 \end{bmatrix}}^{\mathbf{F}_{QP}} + a \overbrace{\begin{bmatrix} v_{rx} \\ v_{ry} \end{bmatrix}}^{\mathbf{V}_{xy}} \tag{16}$$

where $F_1 = f(\dot{Q}_{s\,ref}, |\vec{v}_s|, |\vec{\psi}_s|, Q_{s\,ref}, i_{rx}, w_{sl}, i_{ry})$, $F_2 = f(\dot{P}_{s\,ref}, |\vec{v}_s|, |\vec{\psi}_s|, P_{s\,ref}, i_{rx}, w_{sl}, i_{ry})$, and $a = \frac{3}{2}\frac{L_m}{L_s L_r}|\vec{v}_s|$.

It is possible to relate the new model in (16) to the voltage signals between the midpoints of the converter legs and the DC link, if $\mathbf{D}$ transformation matrix in (12) is applied

$$\dot{\mathbf{S}}_{QP} = \mathbf{F}_{QP} + \overbrace{a\mathbf{D}}^{\mathbf{D}_a} \mathbf{V}_{abc}. \tag{17}$$

It can be noticed that control signals are transformed from *a-b-c* to the stator-flux-oriented reference frame by means of $\mathbf{D}_a$ matrix. Now, it seems logical to derive the $\mathbf{S}$ in (15) by arranging (8) and (9) in matrix format, $\mathbf{S}_{QP} = \begin{bmatrix} s_{Q_s} & s_{P_s} \end{bmatrix}^T$, and then transforming $\mathbf{S}_{QP}$ by means of $\mathbf{D}_a^+$:

$$\mathbf{S} = \mathbf{D}_a^+ \mathbf{S}_{QP}. \tag{18}$$

This allows obtaining the three-phase control signals as:

$$\mathbf{V}_{abc} = u_0 \begin{bmatrix} \mathrm{sgn}(s_{P_s} \sin\rho - s_{Q_s} \cos\rho_s) \\ \mathrm{sgn}(s_{P_s} \sin(\rho - \frac{2\pi}{3}) - s_{Q_s} \cos(\rho - \frac{2\pi}{3})) \\ \mathrm{sgn}(s_{P_s} \sin(\rho + \frac{2\pi}{3}) - s_{Q_s} \cos(\rho + \frac{2\pi}{3})) \end{bmatrix}, \tag{19}$$

where $1/a$ constant should appear multiplying the terms inside every sgn function. However, as its value is always positive, it does not affect the final result, and this is the reason why it has been removed from (19). To conclude, the transistor gating signals are achieved just by replacing (19) in (14).

Due to the discontinuous nature of the generated command signals —which are in fact the transistors' gating signals—, a bumpless transition between synchronization and optimum generation states takes place spontaneously, without requiring the use of further control techniques, as that proposed in (Tapia et al., 2009).

3.1.1.1 Stability proof

In order to confirm that the designed control signals assure the zero-convergence of the switching variables, the following positive-definite Lyapunov function candidate is proposed:

$$V = \frac{1}{2}\mathbf{S}_{QP}^T\mathbf{S}_{QP}, \tag{20}$$

and, as it is well-known, its time derivative must be negative-definite:

$$\dot{V} = \frac{1}{2}\left(\dot{\mathbf{S}}_{QP}^T\mathbf{S}_{QP} + \mathbf{S}_{QP}^T\dot{\mathbf{S}}_{QP}\right) = \mathbf{S}_{QP}^T\dot{\mathbf{S}}_{QP} < 0. \tag{21}$$

Considering (17) and (18), the Lyapunov function time derivative can be rewritten as:

$$\dot{V} = \mathbf{S}^T\mathbf{F} - \frac{4}{9}a^2u_0\begin{bmatrix} s_1 \\ s_2 \\ s_3 \end{bmatrix}^T\begin{bmatrix} \text{sgn}(s_1) - 0.5\text{sgn}(s_2) - 0.5\text{sgn}(s_3) \\ \text{sgn}(s_2) - 0.5\text{sgn}(s_3) - 0.5\text{sgn}(s_1) \\ \text{sgn}(s_3) - 0.5\text{sgn}(s_1) - 0.5\text{sgn}(s_2) \end{bmatrix}, \tag{22}$$

where $\mathbf{F} = \mathbf{D}_a^T\mathbf{F}_{QP} = [F_1^* \; F_2^* \; F_3^*]^T$.

Taking into account that the elements of $\mathbf{V}_{abc}$ will never coincide in sign at every moment, nor will $\mathbf{S}$ components, as it can be inferred from (15). Therefore, $\text{sgn}(s_l) \neq \text{sgn}(s_m) = \text{sgn}(s_n)$, where $l \neq m \neq n$, for $l, m, n \in \{1, 2, 3\}$. Let $l = 1$, $m = 2$ and $n = 3$; moreover, suppose that $\text{sgn}(s_1) = +1 \neq \text{sgn}(s_2) = \text{sgn}(s_3)$, then (22) could be transformed into:

$$\dot{V} = \underbrace{s_1F_1^* + s_2F_2^* + s_3F_3^*}_{p} - \underbrace{\frac{4}{9}a^2u_0\left(2|s_1| + |s_2| + |s_3|\right)}_{q}. \tag{23}$$

If $\dot{V} < 0$ must be guaranteed, it can be stated that $|q| > |p|$. Furthermore, if the most restrictive case is considered, the following condition must be derived:

$$\frac{4}{9}a^2u_0\left(2|s_1| + |s_2| + |s_3|\right) > |s_1||F_1^*| + |s_2||F_2^*| + |s_3||F_3^*|. \tag{24}$$

Comparing each accompanying term of $|s_1|$, $|s_2|$ and $|s_3|$, u_0 can be fixed by guaranteing that

$$u_0 > \frac{9}{4a^2}\max\left(\frac{|F_1^*|}{2}, |F_2^*|, |F_3^*|\right) \tag{25}$$

is satisfied. Nevertheless, bearing in mind the remaining signs combinations between switching functions s_1, s_2 and s_3, and taking into account the most demanding case, the above proposed condition turns out to be:

$$u_0 > \frac{9}{4a^2}\max\left(|F_1^*|, |F_2^*|, |F_3^*|\right). \tag{26}$$

Provided that the controller supplies the convenient voltage, derived from (26), the system is robust even in the presence of disturbances, guarantying thus the asymptotic convergence of s_{Q_s} and s_{P_s} to zero. (26) presents a very conservative condition, but, in practice, a lower value of u_0 is usually enough to assure the stability of the whole system.

3.1.2 DFIG disconnected from the grid —Synchronization stage

When rotor speed-threshold is achieved, the control system activates the synchronization stage. As mentioned before, in order to avoid short circuit, the goal is to match the stator and grid voltages in magnitude and phase by requesting the reference values presented in (5). Let the same multivariable control law structure exposed in (15) be employed, considering, of course, the new subspace where it must be applied. Combining (3) and (4) with the time derivatives of (10) and (11), the model can be transferred to the above-mentioned new subspace $\mathbf{S}_{x'y'} = \begin{bmatrix} s_{i_{rx'}} & s_{i_{ry'}} \end{bmatrix}^T$:

$$\overbrace{\begin{bmatrix} \dot{s}_{i_{rx'}} \\ \dot{s}_{i_{ry'}} \end{bmatrix}}^{\dot{\mathbf{S}}_{x'y'}} = \overbrace{\begin{bmatrix} M_1 \\ M_2 \end{bmatrix}}^{\mathbf{M}_{x'y'}} + b \overbrace{\begin{bmatrix} v_{rx'} \\ v_{ry'} \end{bmatrix}}^{\mathbf{V}_{x'y'}}, \tag{27}$$

where $M_1 = f(\dot{i}_{rx'\,ref}, i_{rx'\,ref}, i_{rx'}, w_{sl}, i_{ry'})$, $M_2 = f(\dot{i}_{ry'\,ref}, i_{ry'\,ref}, i_{ry'}, w_{sl}, i_{rx'})$, and $b = -1/L_r$.

Following a similar procedure to that presented in 3.1.1, the switching variables referred to *a-b-c* reference frame will be obtained as:

$$\mathbf{S} = \mathbf{D}_b^+ \mathbf{S}_{x'y'}, \tag{28}$$

where $\mathbf{D}_b^+$ is the Moore-Penrose pseudo-inverse of $\mathbf{D}_b = b\mathbf{D}$. Substituting (28) in the proposed control law (15), the three-phase command signals to be generated turn out to be:

$$\mathbf{V}_{abc} = u_0 \begin{bmatrix} \operatorname{sgn}(s_{i_{rx'}} \cos\rho' - s_{i_{ry'}} \sin\rho') \\ \operatorname{sgn}(s_{i_{rx'}} \cos(\rho' - \frac{2\pi}{3}) - s_{i_{ry'}} \sin(\rho' - \frac{2\pi}{3})) \\ \operatorname{sgn}(s_{i_{rx'}} \cos(\rho' + \frac{2\pi}{3}) - s_{i_{ry'}} \sin(\rho' + \frac{2\pi}{3})) \end{bmatrix}, \tag{29}$$

where $\rho' = \rho'_s - \theta_r$. The gating signals should easily be achieved by replacing (29) in (14).

3.1.2.1 Stability proof

Analogous to the case in 3.1.1.1, the asymptotic zero-convergence of switching functions is assured if the following condition is accomplished:

$$u_0 > \frac{9}{4b^2} \max\left(|M_1^*|, |M_2^*|, |M_3^*|\right), \tag{30}$$

where $\mathbf{M} = \mathbf{D}_b^T \mathbf{M}_{x'y'} = [M_1^*\ M_2^*\ M_3^*]^T$, and the positive-definite Lyapunov function candidate is selected as:

$$V = \frac{1}{2} \mathbf{S}_{x'y'}^T \mathbf{S}_{x'y'}. \tag{31}$$

3.2 Higher-order sliding-mode controller

The proposed structure based on 1-SMC leads to a variable switching frequency of the RSC transistors (Susperregui et al., 2010), which may inject broadband harmonics into the grid, complicating the design of the back-to-back converter itself, as well as that of the grid-side AC filter (Zhi & Xu, 2007). As an alternative to the 1-SMC, higher-order sliding-mode control (HOSMC) could be adopted. In particular, and owing to the relative order the system presents,

a 2-SMC realization, known as the *super-twisting algorithm* (STA), may be employed (Bartolini et al., 1999; Levant, 1993). The control signal comprises two terms; one guaranteing that switching surface $s = 0$ is reached in finite time, and another related to the integral of the switching variable sign. Namely,

$$u = -\lambda |s|^{\rho} \mathrm{sgn}(s) - w \int \mathrm{sgn}(s) dt, \tag{32}$$

where $\rho = 0.5$ assures a real second-order sliding-mode. This technique gives rise to a continuous control signal, which not only alleviates or completely removes the "chatter" from the system, but must also be modulated. To this effect, SVM may be applied, therefore obtaining a fixed switching frequency which results in elimination of the above-mentioned drawback.
As previously remarked, two controllers must be designed in order to command the performance of the DFIG when connected and disconnected from the grid.

3.2.1 DFIG connected to the grid —Optimum power generation

Considering the time derivatives of (8) and (9) together with expressions (3), (4) and (7), it turns out that

$$\dot{s}_{Q_s} = \dot{Q}_{s\ ref} - \frac{3}{2}\frac{1}{L_s}|\vec{v}_s| \left[c_Q |\vec{\psi}_s| + \left(\frac{R_r}{L'_r} - c_Q \right) L_m i_{rx} - \omega_{sl} L_m i_{ry} \right] + c_Q Q_{s\ ref} + \\ + \frac{3}{2}\frac{L_m}{L_s L'_r}|\vec{v}_s| v_{rx} \tag{33}$$

$$\dot{s}_{P_s} = \dot{P}_{s\ ref} + \frac{3}{2}\frac{L_m}{L_s}|\vec{v}_s| \left[\left(c_P - \frac{R_r}{L'_r} \right) i_{ry} - \omega_{sl} i_{rx} - \omega_{sl} \frac{L_m}{L_s L'_r} |\vec{\psi}_s| \right] + c_P P_{s\ ref} + \\ + \frac{3}{2}\frac{L_m}{L_s L'_r}|\vec{v}_s| v_{ry}, \tag{34}$$

where $\frac{d|\vec{\psi}_s|}{dt}$ has been neglected due to the fact that the DFIG is grid connected. Aiming to track the optimum power curve, the voltage to be applied to the rotor may be derived according to control law

$$v_{rx} = v_{rx_{ST}} + v_{rx_{eq}}; \;\; v_{ry} = v_{ry_{ST}} + v_{ry_{eq}}, \tag{35}$$

where the terms with subscript 'ST' are computed, through application of the STA, as:

$$v_{rx_{ST}} = \frac{2}{3}\frac{L_s L'_r}{|\vec{v}_s| L_m} \left[-\lambda_Q |s_{Q_s}|^{0.5} \mathrm{sgn}(s_{Q_s}) - w_Q \int \mathrm{sgn}(s_{Q_s}) dt \right] \tag{36}$$

$$v_{ry_{ST}} = \frac{2}{3}\frac{L_s L'_r}{|\vec{v}_s| L_m} \left[-\lambda_P |s_{P_s}|^{0.5} \mathrm{sgn}(s_{P_s}) - w_P \int \mathrm{sgn}(s_{P_s}) dt \right] \tag{37}$$

with λ_Q, w_Q, λ_P and w_P being positive parameters to be tuned. The gain premultiplying the algorithms —the inverse of that affecting control signal in (33) and (34)— is exclusively applied for assisting in the process of tuning the foregoing parameters. The addends with subscript '*eq*' in (35), which correspond to equivalent control terms, are derived by letting $\dot{s}_{P_s} = \dot{s}_{Q_s} = 0$ (Utkin et al., 1999). As a result,

$$v_{rx_{eq}} = -\frac{2}{3}\frac{L_s L'_r}{|\vec{v}_s| L_m} \left[\dot{Q}_{s\ ref} + c_Q (Q_{s\ ref} - Q_s) \right] + R_r i_{rx} - L'_r \omega_{sl} i_{ry} \tag{38}$$

$$v_{ry_{eq}} = -\frac{2}{3}\frac{L_s L'_r}{|\vec{v}_s| L_m} \left[\dot{P}_{s\ ref} + c_P (P_{s\ ref} - P_s) \right] + R_r i_{ry} + \frac{L_m}{L_s} \omega_{sl} |\vec{\psi}_s| + L'_r \omega_{sl} i_{rx}. \tag{39}$$

It should be noted that sliding regime in manifold $s_{P_s} = s_{Q_s} = \dot{s}_{P_s} = \dot{s}_{Q_s} = 0$ can also be attained by applying only the control terms in (35) corresponding to the STA. Accordingly, the equivalent control terms in (38) and (39) are not strictly necessary, but, once included, the more accurately they are computed, the lower is the control effort let to be done by the STA. Equivalent control terms are hence incorporated not only to improve the system transient response (Rashed et al., 2005), but also to ease selection of constants c_P and c_Q, as well as tuning of the STA $\lambda_{Q,P}$ and $w_{Q,P}$ gains.
In effect, substituting control law (35) into (33) and (34) produces:

$$\dot{s}_{Q_s} = -\lambda_Q \left|s_{Q_s}\right|^{0.5} \operatorname{sgn}(s_{Q_s}) - w_Q \int \operatorname{sgn}(s_{Q_s})\, dt \tag{40}$$

$$\dot{s}_{P_s} = -\lambda_P \left|s_{P_s}\right|^{0.5} \operatorname{sgn}(s_{P_s}) - w_P \int \operatorname{sgn}(s_{P_s})\, dt. \tag{41}$$

Now, given that $\operatorname{sgn}(s) = s/|s|$, taking the time derivatives of (40) and (41) leads to:

$$\ddot{s}_{Q_s} = -0.5\lambda_Q \left|s_{Q_s}\right|^{-0.5} \dot{s}_{Q_s} - w_Q \left|s_{Q_s}\right|^{-1} s_{Q_s} \tag{42}$$

$$\ddot{s}_{P_s} = -0.5\lambda_P \left|s_{P_s}\right|^{-0.5} \dot{s}_{P_s} - w_P \left|s_{P_s}\right|^{-1} s_{P_s}. \tag{43}$$

Let us assume that, thanks to the first addend in the STA, the reaching phase is satisfactorily completed and the sliding regime is entered. From that moment on, $\left|s_{Q_s,P_s}\right| \leq \delta_{Q,P}$, with $\delta_{Q,P}$ close to zero. Considering the most unfavorable case, in which $\left|s_{Q_s,P_s}\right| = \delta_{Q,P}$, and using the definition of s_{Q_s,P_s} in (8) and (9), the following expressions can respectively be worked out from (42) and (43):

$$\ddot{e}_Q + \overbrace{\left(0.5\delta_Q^{-0.5}\lambda_Q + c_Q\right)}^{a_2(c_Q,\,\lambda_Q)} \dot{e}_Q + \overbrace{\left(0.5\delta_Q^{-0.5}\lambda_Q c_Q + \delta_Q^{-1} w_Q\right)}^{a_1(c_Q,\,\lambda_Q,\,w_Q)} e_Q + \overbrace{\delta_Q^{-1} w_Q c_Q}^{a_0(c_Q,\,w_Q)} \int e_Q dt = 0 \tag{44}$$

$$\ddot{e}_P + \overbrace{\left(0.5\delta_P^{-0.5}\lambda_P + c_P\right)}^{b_2(c_P,\,\lambda_P)} \dot{e}_P + \overbrace{\left(0.5\delta_P^{-0.5}\lambda_P c_P + \delta_P^{-1} w_P\right)}^{b_1(c_P,\,\lambda_P,\,w_P)} e_P + \overbrace{\delta_P^{-1} w_P c_P}^{b_0(c_P,\,w_P)} \int e_P dt = 0. \tag{45}$$

Taking the time derivatives of (44) and (45), the following differential equations reflecting the e_Q and e_P error dynamics while in sliding regime are obtained:

$$\dddot{e}_Q + a_2\ddot{e}_Q + a_1\dot{e}_Q + a_0 e_Q = 0 \tag{46}$$

$$\dddot{e}_P + b_2\ddot{e}_P + b_1\dot{e}_P + b_0 e_P = 0. \tag{47}$$

Hence, once $\delta_{Q,P}$ is fixed, adequate selection of $c_{Q,P}$, $\lambda_{Q,P}$ and $w_{Q,P}$ allows attaining certain target error dynamics established through the third-order characteristic equation given next:

$$\left(p^2 + 2\xi\omega_n p + \omega_n^2\right)(p + \alpha\xi\omega_n) = p^3 + \underbrace{(2+\alpha)\,\xi\omega_n}_{d_2} p^2 + \underbrace{\left(1 + 2\alpha\xi^2\right)\omega_n^2}_{d_1} p + \underbrace{\alpha\xi\omega_n^3}_{d_0} = 0 \tag{48}$$

which, provided that α is selected high enough —typically $\alpha \geq 10$—, gives rise to a pair of dominant poles with respect to a third one placed at $p = -\alpha\xi\omega_n$. As a result, it can be considered that target error dynamics are entirely defined via ξ damping coefficient and ω_n natural frequency. Those designer-defined error dynamics would theoretically be

achieved just by tuning $c_{Q,P}$, $\lambda_{Q,P}$ and $w_{Q,P}$ so that $a_2 = d_{2Q}(\xi_Q, \omega_{nQ})$, $a_1 = d_{1Q}(\xi_Q, \omega_{nQ})$, $a_0 = d_{0Q}(\xi_Q, \omega_{nQ})$, $b_2 = d_{2P}(\xi_P, \omega_{nP})$, $b_1 = d_{1P}(\xi_P, \omega_{nP})$ and $b_0 = d_{0P}(\xi_P, \omega_{nP})$ are simultaneously fulfilled. Note that both ξ and ω_n could in general take different values if different dynamic behaviours for reactive and active power errors were required.
Considering the expressions for a_2, a_1, a_0, b_2, b_1 and b_0 provided in (44) and (45), as well as those for d_2, d_1 and d_0 reflected in (48), the latter conditions lead to the following tuning equations:

$$c_Q^3 - d_{2Q}c_Q^2 + d_{1Q}c_Q - d_{0Q} = 0;\ c_P^3 - d_{2P}c_P^2 + d_{1P}c_P - d_{0P} = 0 \tag{49}$$

$$\lambda_Q = 2\left(d_{2Q} - c_Q\right)\delta_Q^{0.5};\ \lambda_P = 2\left(d_{2P} - c_P\right)\delta_P^{0.5} \tag{50}$$

$$w_Q = \left[d_{1Q} - c_Q(d_{2Q} - c_Q)\right]\delta_Q;\ w_P = \left[d_{1P} - c_P(d_{2P} - c_P)\right]\delta_P. \tag{51}$$

It is important to note that the coefficients in (49) coincide with those of target characteristic equation (48), except for the signs of the squared and independent terms, which are negative. It therefore turns out that the three possible values for $c_{Q,P}$ are equal to the roots —poles— of target characteristic equation (48), although their real parts have opposite signs. Since the real parts of the desired poles must necessarily be negative to ensure stability, the latter implies that the real parts of the three possible values for $c_{Q,P}$ will always be positive. As a result, given that expressions in (49) are third-order equations, it is guaranteed that at least one of the three solutions for $c_{Q,P}$ will be both real and positive, as required.
Specifically, depending on the value chosen for $\xi_{Q,P}$, one of the following three cases arises:

1. If $0 < \xi_{Q,P} < 1$, only one of the three solutions for $c_{Q,P}$ is both real and positive, $c_{Q,P} = \alpha\xi_{Q,P}\omega_{nQ,P}$.
2. If $\xi_{Q,P} = 1$, two different acceptable solutions for $c_{Q,P}$ are obtained, $c_{1Q,P} = \omega_{nQ,P}$ and $c_{2Q,P} = \alpha\omega_{nQ,P}$.
3. If $\xi_{Q,P} > 1$, the three solutions for $c_{Q,P}$ are real and positive, $c_{1Q,P} = \omega_{nQ,P}\left(\xi_{Q,P} - \sqrt{\xi_{Q,P}^2 - 1}\right)$, $c_{2Q,P} = \omega_{nQ,P}\left(\xi_{Q,P} + \sqrt{\xi_{Q,P}^2 - 1}\right)$ and $c_{3Q,P} = \alpha\xi_{Q,P}\omega_{nQ,P}$.

For cases 2 and 3, two or three possible sets of values for $c_{Q,P}$, $\lambda_{Q,P}$ and $w_{Q,P}$ are respectively obtained. The set of parameters leading to the best performance may, for example, be identified through simulation.

3.2.2 DFIG disconnected from the grid —Synchronization stage

The design and tuning process of the current controllers, which synchronizes the voltage induced at the open stator to that of the grid, is analogous to that presented in the preceding section 3.2.1. Let the control law with respect to x'-y' reference frame be

$$v_{rx'} = v_{rx'_{ST}} + v_{rx'_{eq}};\ v_{ry'} = v_{ry'_{ST}} + v_{ry'_{eq}}. \tag{52}$$

Taking the time derivatives of (10) and (11), the expressions given next arise if (3) and (4) are considered:

$$\dot{s}_{i_{rx'}} = \dot{i}_{rx'\,ref} + c_{rx'}\dot{i}_{rx'\,ref} + \left(\frac{R_r}{L_r} - c_{rx'}\right)i_{rx'} - \omega_{sl}i_{ry'} - \frac{1}{L_r}v_{rx'} \tag{53}$$

$$\dot{s}_{i_{ry'}} = \dot{i}_{ry'\,ref} + c_{ry'}\dot{i}_{ry'\,ref} + \left(\frac{R_r}{L_r} - c_{ry'}\right)i_{ry'} + \omega_{sl}i_{rx'} - \frac{1}{L_r}v_{ry'}. \tag{54}$$

The terms corresponding to the STA may be obtained as

$$v_{rx'_{ST}} = L_r \left[\lambda_{x'} |s_{i_{rx'}}|^{0.5} \text{sgn}(s_{i_{rx'}}) + w_{x'} \int \text{sgn}(s_{i_{rx'}}) dt \right] \tag{55}$$

$$v_{ry'_{ST}} = L_r \left[\lambda_{y'} |s_{i_{ry'}}|^{0.5} \text{sgn}(s_{i_{ry'}}) + w_{y'} \int \text{sgn}(s_{i_{ry'}}) dt \right], \tag{56}$$

where $\lambda_{x'}$, $w_{x'}$, $\lambda_{y'}$ and $w_{y'}$ are positive parameters to be tuned. As far as equivalent control terms are concerned, they are derived by zeroing (53) and (54), thus yielding

$$v_{rx'_{eq}} = L_r \left[\dot{i}_{rx'\,ref} + \frac{R_r}{L_r} i_{rx'} - \omega_{sl} i_{ry'} + c_{rx'} (i_{rx'\,ref} - i_{rx'}) \right] \tag{57}$$

$$v_{ry'_{eq}} = L_r \left[\dot{i}_{ry'\,ref} + \frac{R_r}{L_r} i_{ry'} + \omega_{sl} i_{rx'} + c_{ry'} (i_{ry'\,ref} - i_{ry'}) \right]. \tag{58}$$

Again, note that all the control terms are premultiplied by a $-L_r$ gain in this case, which is the inverse of that affecting control signals in (53) and (54). As mentioned before, its only purpose is to facilitate the tuning of the parameters involved in the commanding algorithm.
Substitution of control law (52) into (53) and (54) leads to

$$\dot{s}_{i_{rx'}} = -\lambda_{x'} |s_{i_{rx'}}|^{0.5} \text{sgn}(s_{i_{rx'}}) - w_{x'} \int \text{sgn}(s_{i_{rx'}}) dt \tag{59}$$

$$\dot{s}_{i_{ry'}} = -\lambda_{y'} |s_{i_{ry'}}|^{0.5} \text{sgn}(s_{i_{ry'}}) - w_{y'} \int \text{sgn}(s_{i_{ry'}}) dt, \tag{60}$$

expressions which turn out to be identical to those presented in (40) and (41) provided that '$i_{rx'}$' and 'x'' subscripts are respectively replaced by 'Q_s' and 'Q', and, likewise, '$i_{ry'}$' and 'y'' subscripts are interchanged with 'P_s' and 'P'. Therefore, the same reasoning detailed in section 3.2.1 can be followed in order to achieve the tuning equations of $\lambda_{x'}$, $w_{x'}$, $c_{x'}$, $\lambda_{y'}$, $w_{y'}$ and $c_{y'}$ parameters. As a result,

$$c_{x'}^3 - d_{2x'} c_{x'}^2 + d_{1x'} c_{x'} - d_{0x'} = 0;\ c_{y'}^3 - d_{2y'} c_{y'}^2 + d_{1y'} c_{y'} - d_{0y'} = 0 \tag{61}$$

$$\lambda_{x'} = 2 \left(d_{2x'} - c_{x'} \right) \delta_{x'}^{0.5};\ \lambda_{y'} = 2 \left(d_{2y'} - c_{y'} \right) \delta_{y'}^{0.5} \tag{62}$$

$$w_{x'} = \left[d_{1x'} - c_{x'} (d_{2x'} - c_{x'}) \right] \delta_{x'};\ w_{y'} = \left[d_{1y'} - c_{y'} (d_{2y'} - c_{y'}) \right] \delta_{y'} \tag{63}$$

3.2.3 Bumpless connection

Considering that the DFIG presents different dynamics when disconnected or connected to the grid, two STA-based controllers have been designed for generating a continuous command signal. So far, the performance for each state has only been considered, but undesirable phenomena may appear if the switch between the two controllers is not properly carried out. If a direct transition is accomplished, a discontinuity arises in the command signal at the instant of connection, due to the magnitude mismatch between the rotor voltages generated by the two controllers. This effect produces high stator current values, leading the machine to an excessive power exchange with the grid. Aiming to avoid this "bump", it is possible to apply the same value of the control signal previous to and just after the transition —$k-1$ and k instants respectively—; i.e.,

$$v_{rx} = v_{rx'} \tag{64}$$

$$v_{ry} = v_{ry'}. \tag{65}$$

However, this way the "bump" is only delayed one sample time and it actually takes effect in the next sampling instant —$k+1$.
A bumpless transition may take place if the above proposed solution is slightly modified (Åström & Hägglund, 1995). Setting the focus on the rotor voltage components when the DFIG is connected to the grid, appropriate combination of (36), (38) and (37), (39) produces

$$v_{rx} = -\frac{2}{3}\frac{L_s L'_r}{|\vec{v}_s| L_m}\left[\lambda_Q |s_{Q_s}|^{0.5}\mathrm{sgn}(s_{Q_s}) + w_Q \int \mathrm{sgn}(s_{Q_s})dt + \dot{Q}_{s\ ref} + c_Q(Q_{s\ ref} - Q_s)\right] + \\ + R_r i_{rx} - L'_r \omega_{sl} i_{ry} \tag{66}$$

$$v_{ry} = -\frac{2}{3}\frac{L_s L'_r}{|\vec{v}_s| L_m}\left[\lambda_P |s_{P_s}|^{0.5}\mathrm{sgn}(s_{P_s}) + w_P \int \mathrm{sgn}(s_{P_s})dt + \dot{P}_{s\ ref} + c_P(P_{s\ ref} - P_s)\right] + \\ + R_r i_{ry} + \frac{L_m}{L_s}\omega_{sl}|\vec{\psi}_s| + L'_r \omega_{sl} i_{rx}. \tag{67}$$

Two integral terms, $I_{sgn(s_{Q_s})} = \int \mathrm{sgn}(s_{Q_s})dt$ and $I_{sgn(s_{P_s})} = \int \mathrm{sgn}(s_{P_s})dt$, can be observed. Their initial values, which are set to zero when connection occurs, are the source of the mentioned "bump". Aiming at lessening or even eliminating this effect, it can be taken advantage of (64) and (65) to calculate those initial values at connection time. Substituting (66) and (67) into (64) and (65), respectively, leads to

$$I_{\mathrm{sgn}(s_{Q_s})_0} = -\frac{3}{2}\frac{|\vec{v}_s| L_m}{L_s L'_r w_Q}\left(v_{rx'} - R_r i_{rx} + L'_r \omega_{sl} i_{ry}\right) - \\ - \frac{\lambda_Q |s_{Q_s}|^{0.5}\mathrm{sgn}(s_{Q_s}) + \dot{Q}_{s\ ref} + c_Q(Q_{s\ ref} - Q_s)}{w_Q} \tag{68}$$

$$I_{\mathrm{sgn}(s_{P_s})_0} = -\frac{3}{2}\frac{|\vec{v}_s| L_m}{L_s L'_r w_P}\left(v_{ry'} - R_r i_{ry} - \frac{L_m}{L_s}\omega_{sl}|\vec{\psi}_s| - L'_r \omega_{sl} i_{rx}\right) - \\ - \frac{\lambda_P |s_{P_s}|^{0.5}\mathrm{sgn}(s_{P_s}) + \dot{P}_{s\ ref} + c_P(P_{s\ ref} - P_s)}{w_P}. \tag{69}$$

3.3 Sensorless scheme —Adaptation for synchronization

Both the 1-SMC and 2-SMC designs are combined with the MRAS observer proposed by (Peña et al., 2008) in order to build two alternative sensorless control schemes. As a result, the controller is provided with the estimated rotor electrical speed and position, thus avoiding both the use of mechanical components —encoders— and the initial rotor positioning required for the synchronization of the stator and grid voltages (Tapia et al., 2009). Morover, observers may be used for “chattering” phenomenon alleviation (Utkin et al., 1999; Utkin, 1993).
It is worth pointing out that the MRAS observer must be adapted for the case of being disconnected from the grid. On the one hand, since stator currents are null in this state, calculation of stator flux in the stationary s_D-s_Q frame must be slightly modified

$$\psi_{sQ} = \int (v_{sQ} - R_s i_{sQ})dt \rightarrow \psi_{sQ} = \int v_{sQ} dt \tag{70}$$

$$\psi_{sD} = \int (v_{sD} - R_s i_{sD})dt \rightarrow \psi_{sD} = \int v_{sD} dt. \tag{71}$$

On the other hand, the stator voltages are those induced by the rotor currents for synchronization, and present a considerable noise. For a proper control, the affected signals

are filtered out by means of a 500-Hz bandwidth second-order Butterworth filter, which in turn produces a phase lag of $\gamma = 8.1297^\circ$ at 50Hz. This lag must be compensated in order to estimate the components of the actual stator voltage phasor. Considering Fig. 5, it can be stated that

$$|\vec{v}_s| = |\vec{v}_{s\ filtered}| = \sqrt{v^2_{sD\ filtered} + v^2_{sQ\ filtered}} \tag{72}$$

$$\beta = \arctan \frac{v_{sQ\ filtered}}{v_{sD\ filtered}}. \tag{73}$$

Furthermore, given that the γ phase lag is known deriving the argument of $\vec{v}_s$ from Fig. 5 as $\arg(\vec{v}_s) = \beta + \gamma$, the components of the actual stator voltage space-phasor given next arise:

$$v_{sD} = |\vec{v}_s| \cos(\beta + \gamma) \tag{74}$$

$$v_{sQ} = |\vec{v}_s| \sin(\beta + \gamma). \tag{75}$$

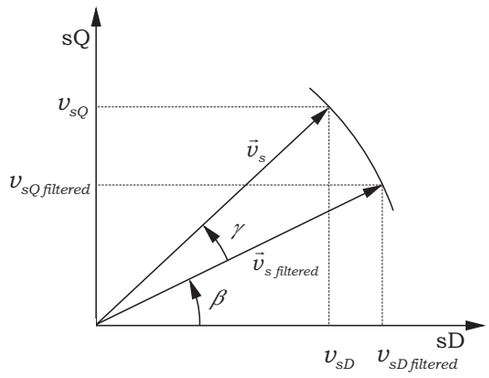

Fig. 5. Actual and filtered stator voltage space-phasors

4. Hardware-in-the-loop results

The presented sensorless 1-SMC and 2-SMC algorithms are evaluated, through real-time HIL emulation, over a full-detail virtual DFIG prototype running on eMEGAsim OP4500 F11-13 simulator by OPAL-RT. The electric parameters of the 660-kW DFIG under consideration are collected in Table 1.

Aiming at showing some of the most illustrative results of the two alternative control algorithms put forward, the test whose main events are reflected in Table 2 is conducted. It should be pointed out that what causes the DFIG control system to generate the order of connection to the grid, taking place at second 0.474, is the DFIG rotational speed exceeding the already mentioned threshold of 1270 rpm.

The 1-SMC algorithm itself is implemented on a Virtex-II Pro series FPGA by Xilinx, which allows reaching the 40-kHz sampling rate required to avoid causing excessive chatter. Direct measurement of the grid voltage allows accurately computing angle ρ'_s, and, as a result, identifying the exact position of the x'-y' reference frame. On the other hand, the ρ_s angle, which provides the location of the stator-flux-oriented x-y reference frame, is derived from the direct (ψ_{sD}) and quadrature (ψ_{sQ}) stationary-frame components of the stator flux. These are in turn estimated by integration of the stator voltage minus the resistive drop. A digital bandpass filter is used as a modified integrator to avoid drift (Peña et al., 2008). Regarding

PARAMETER	VALUE
Rated r.m.s. stator voltage	398/690 V
Rated peak rotor voltage	380 V
Rated peak rotor current	400 A
Stator resistance per phase, R_s	6.7 mΩ
Stator inductance per phase, L_s	7.5 mH
Magnetizing inductance, L_m	19.4 mH
Rotor resistance per phase, R_r	39.9 mΩ
Rotor inductance per phase, L_r	52 mH
General turns ratio, n	0.3806
Number of pole pairs, P	2

Table 1. DFIG electric parameters

EVENT	TIME INSTANT (S)
Order of connection to the grid; start of synchronization process; initial convergence of the observer	0.474
End of synchronization process; connection to the grid at zero power	1.474
Start of power generation	1.974
Sudden increase of wind speed	7
Sudden decrease of wind speed	12

Table 2. Main events of the designed test

switching variables, in this particular case, c_Q and c_P are set to 10, while $c_{x'}$ and $c_{y'}$ are made equal to 0. In addition, the integral terms in s_{P_s} and s_{Q_s} are discretized by applying Tustin's trapezoidal method (Kuo, 1992).

Fig. 6(a) displays a general portrait of the synchronization stage. In addition, details at both its beginning and its end are reflected in Figs. 6(b) and 6(c), respectively. The former evidences the rapid dynamic response of v_{sA}, v_{sB} and v_{sC} voltages, induced at the terminals of the DFIG open stator, when synchronizing with $v_{grid\,A}$, $v_{grid\,B}$ and $v_{grid\,C}$ grid voltages. As expected, no active and reactive powers are exchanged between the DFIG stator and the grid during synchronization, as corroborated by Figs. 7(a) and 7(b).

The DFIG is then connected to the grid at zero power, until power generation according to the optimum power curve is launched 0.5 s later. Fig. 7(a) shows the excellent performance of the stator-side active power, P_s, when, as a result of the two sudden wind speed changes occurring at seconds 7 and 12, a great part of the optimum power curve is tracked both up and downwards. The also superior tracking of the target stator-side reactive power, $Q_{s\,ref}$, is evidenced in Fig. 7(b). The instantaneous reference value for Q_s is fixed so that the DFIG operates with a 0.95 leading —capacitive— power factor all through the test. Chatter in P_s and Q_s represents only ±3% of the rated power.

Given that, as indicated above, control signals are updated at a 40-kHz sample rate, gating signals s_{wk}; $k = 1, 2 \ldots 6$, are able to toggle every 25 μs, if required. This results in a maximum switching frequency of 20 kHz with 50% duty cycle. However, switching frequency of the RSC insulated gate bipolar transistors (IGBTs) is variable, as dictated by switching functions s_1, s_2 and s_3. This is clearly observable in Fig. 8(a), where the frequency spectrum corresponding to

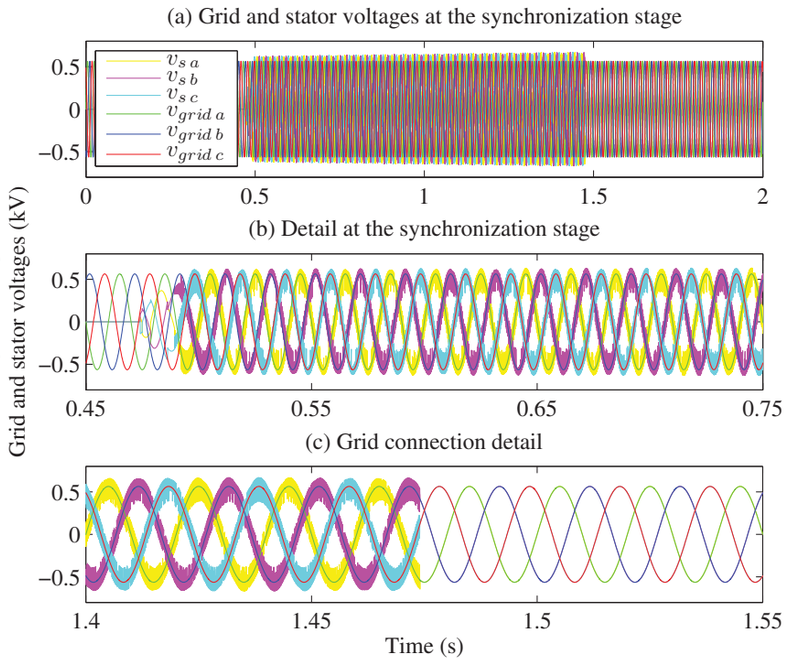

Fig. 6. Stator and grid voltages of the 1-SMC controller-driven DFIG at the synchronization stage

gating signal s_{w1} is displayed. The three-phase rotor current resulting from the gating signals applied to the RSC IGBTs is that displayed in Fig. 8(b). As expected, it turns out to be variable in magnitude, frequency and phase.

Fig. 9 reflects the performance of the digital MRAS observer, which operates at a 1-kHz sample rate. In this particular case, it is incorporated not only for sensorless control, but also as a supporting tool for chatter attenuation (Utkin et al., 1999; Utkin, 1993). The observer is launched once the order of connection to the grid is automatically generated. As evidenced in Fig. 9(a), the estimated rotor mechanical speed converges rapidly to its actual value at the earlier part of the synchronization stage, and, from that point onwards, keeps track of it satisfactorily in spite of the transition from the disconnected state to the connected one taking place at second 1.474. Moreover, a detail illustrating the fast convergence of the estimated rotor electrical position to its actual value is displayed in Fig. 9(b).

As far as the sensorless 2-SMC algorithm is concerned, it is programmed in C language on a DSP-based board. Control signals v_{rx} and v_{ry} are demodulated to derive the $v_{r\alpha}$ and $v_{r\beta}$ voltage components, expressed in the rotor natural reference frame, which are then supplied as inputs to the SVM algorithm generating the gating signals of RSC IGBTs. Angles ρ_s and ρ_s', required both to estimate equivalent control terms and to demodulate v_{rx} and v_{ry} control signals, are derived in the same manner as for the 1-SMC algorithm. Both the 2-SMC and SVM algorithms operate at a 5-kHz sample rate, while the MRAS observer runs, as in the preceding case, at 1 kHz. The integral terms included in both the switching functions and the STA algorithm itself are digitally implemented based on Tustin's trapezoidal method. Yet, aiming to elude the risk of causing derivative "ringing" (Åström & Hägglund, 1995), Euler's rectangular method is applied to discretize the time derivatives of $P_{s\,ref}$ and $Q_{s\,ref}$ appearing in equivalent control terms.

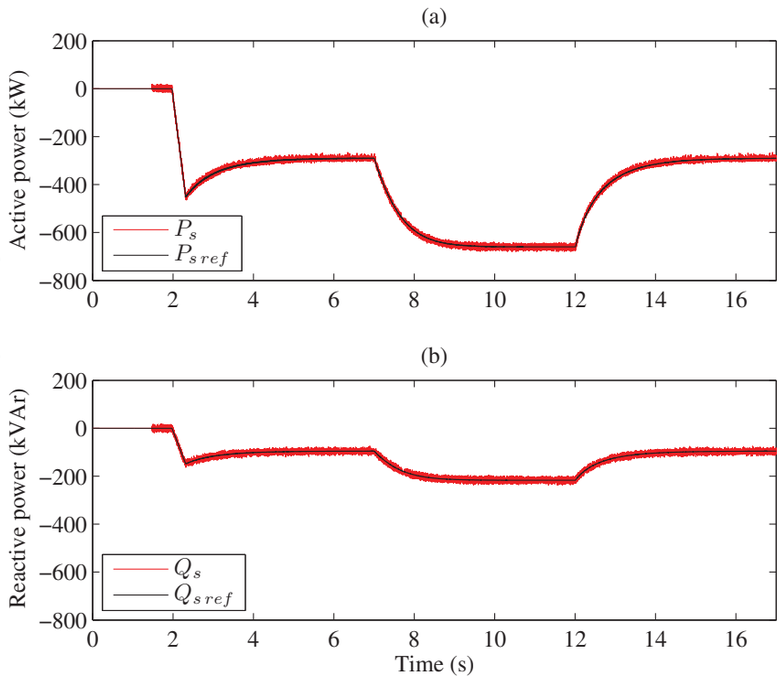

Fig. 7. Active and reactive powers of the DFIG commanded by the 1-SMC controller

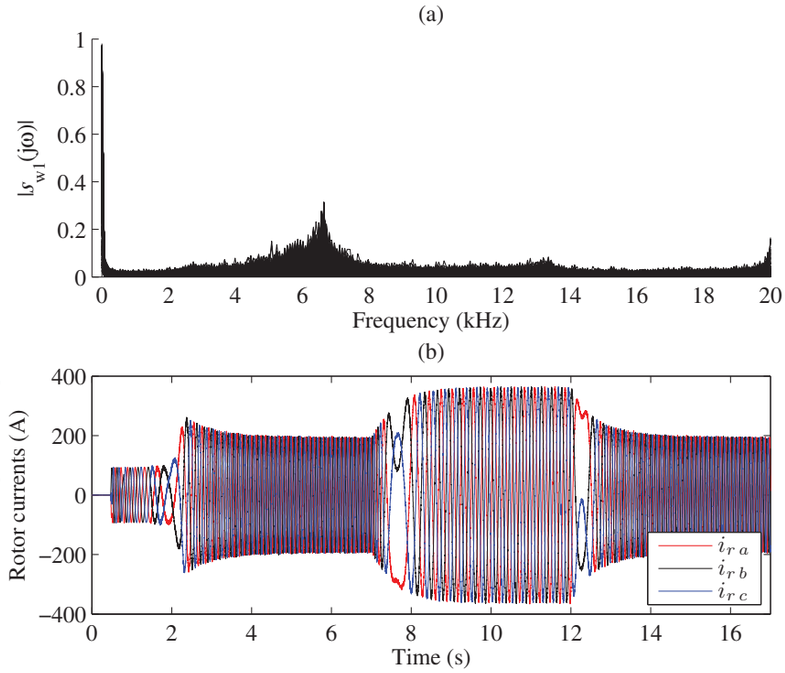

Fig. 8. Frequency spectrum of s_{w1} gating signal, and resulting three-phase rotor current

Selecting a $\delta_{x',y'} = 0.01$ A, control parameters for synchronization are adjusted seeking to reach closed-loop rotor current error dynamics exhibiting a unit damping coefficient and a $\omega_{nx',y'} = 55.2381$ rad/s natural frequency while in sliding regime. As a result, if different

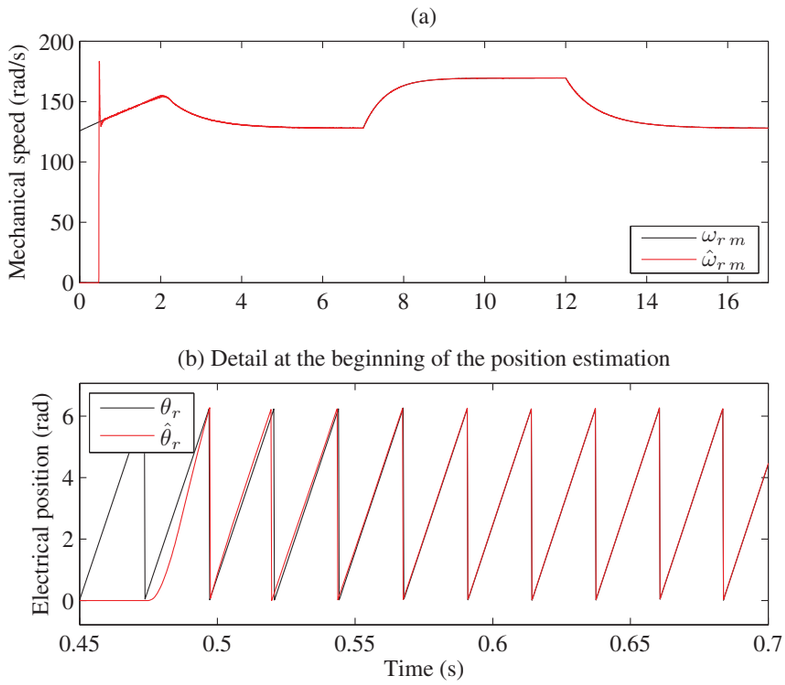

Fig. 9. Actual and estimated mechanical speed and electrical position of the DFIG rotor

from zero, errors in rotor current $i_{rx'}$ and $i_{ry'}$ components would vanish, according to the 2% criterion (Ogata, 2001), in 105 ms, showing no overshoots. Similarly, forcing $\delta_{P,Q}$ to be equal to 0.1 kW, and specifying $\xi_{P,Q} = 1$ and $\omega_{nP,Q} = 82.8571$ rad/s, respectively, as target damping coefficient and natural frequency for closed-loop power error dynamics, possible errors arising in active and reactive powers would theoretically decay to zero in 70 ms, with no overshoots. If α is made equal to 10, the values resulting for the 2-SMC algorithm parameters are those collected in Table 3.

PARAMETER	VALUE
$c_{x'}$, $c_{y'}$	55.2381
$\lambda_{x'}$, $\lambda_{y'}$	121.5238
$w_{x'}$, $w_{y'}$	305.1247
c_P, c_Q	82.8571
λ_P, λ_Q	$1.8229 \cdot 10^4$
w_P, w_Q	$6.8653 \cdot 10^6$

Table 3. Values for the parameters belonging to the 2-SMC algorithm

The most significant results corresponding to the applied sensorless SVM-based 2-SMC are illustrated by Figs. 10, 11 and 12. Given that those figures are very similar to their corresponding 1-SMC counterparts —Figs. 6, 7 and 8, respectively—, only the main differences between them will accordingly be commented on.
Comparison of Figs. 6 and 7 with Figs. 10 and 11, respectively, reveals that the resulting chatter is somewhat lower for the 2-SMC case. In addition, synchronization of the voltage induced in the DFIG open stator to that of the grid is achieved faster when applying the 1-SMC algorithm,

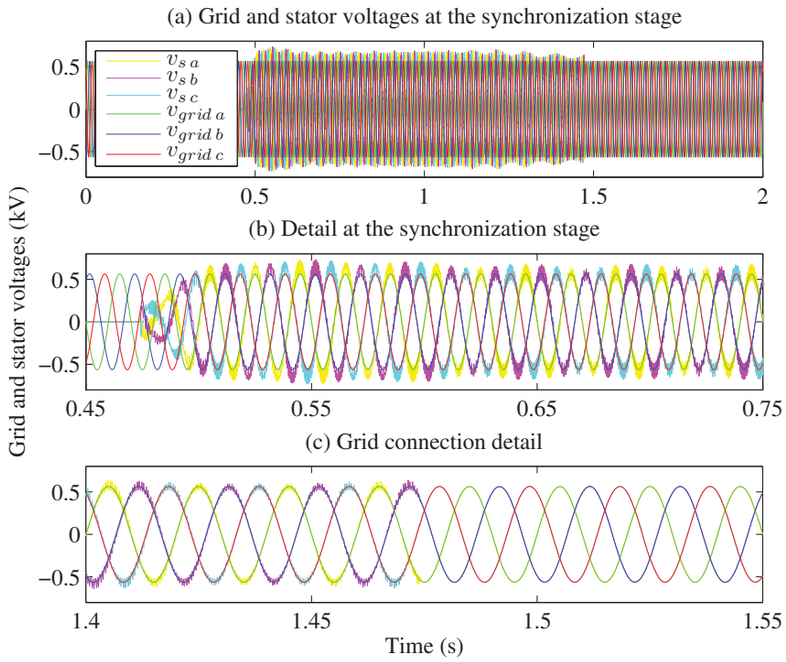

Fig. 10. Stator and grid voltages of the 2-SMC controller-driven DFIG at the synchronization stage

as evidenced by Figs. 6 and 10. Furthermore, even though the 2-SMC algorithm is provided with bumpless transfer from the disconnected state to the connected one, Figs. 7 and 11 prove that power exchange with the grid at the instant of connection is considerably lower for the case of the 1-SMC.

On the other hand, since the SVM-based 2-SMC leads to a 5-kHz constant switching frequency of the RSC IGBTs, in Fig. 12(a) the frequency spectrum of Fig. 8(a) has been replaced with the $v_{r\alpha}$ and $v_{r\beta}$ voltage components supplied as inputs to the SVM algorithm. The smoothness of $v_{r\alpha}$ and $v_{r\beta}$ in Fig. 12(a) indicates that, like in classical PI controller-based FOC schemes, chatter in P_s and Q_s observable in Fig. 11 is just attributable to SVM, not to the 2-SMC algorithm itself.

To conclude, as it turns out that the MRAS observer performance is extremely similar to that resulting in the case of the sensorless 1-SMC, it is not included here to avoid reiteration.

5. Conclusion

Real-time HIL emulation results obtained by running sensorless versions of the 1-SMC and 2-SMC arrangements presented in this chapter reveal that excellent tracking of a predefined rotor speed-dependent optimum power curve is reached in both cases. In addition, prior to connecting the DFIG stator to the grid, they are also capable of achieving satisfactory synchronization of the voltage induced at the open stator terminals to that of the grid.

In any case, it may be of interest to contrast both SMC algorithms, so as to identify the strengths and weaknesses associated to each of them. This section will hence focus on that comparison.

As far as the complexity of the algorithm itself is concerned, the 1-SMC version turns out to be considerably simpler than the 2-SMC one. Given that the control signals generated

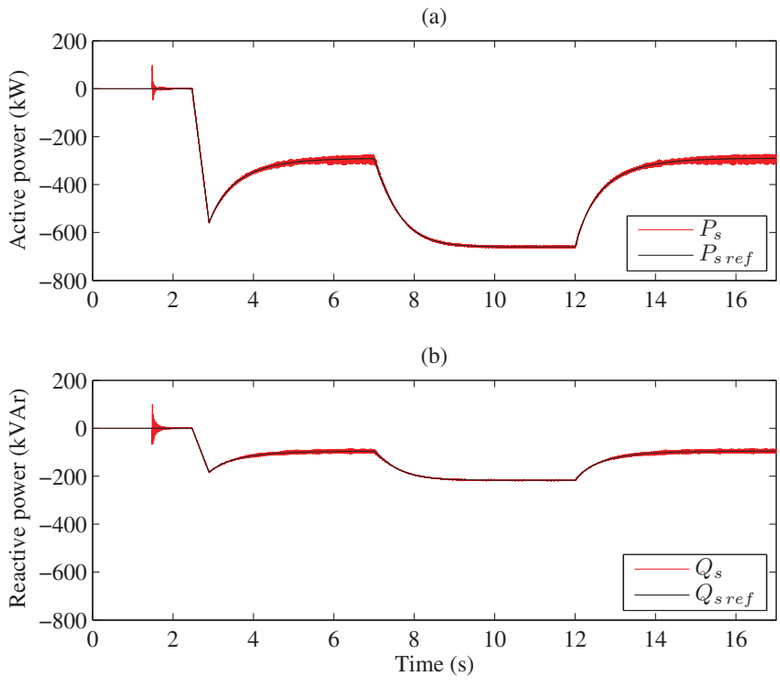

Fig. 11. Active and reactive powers of the DFIG commanded by the 2-SMC controller

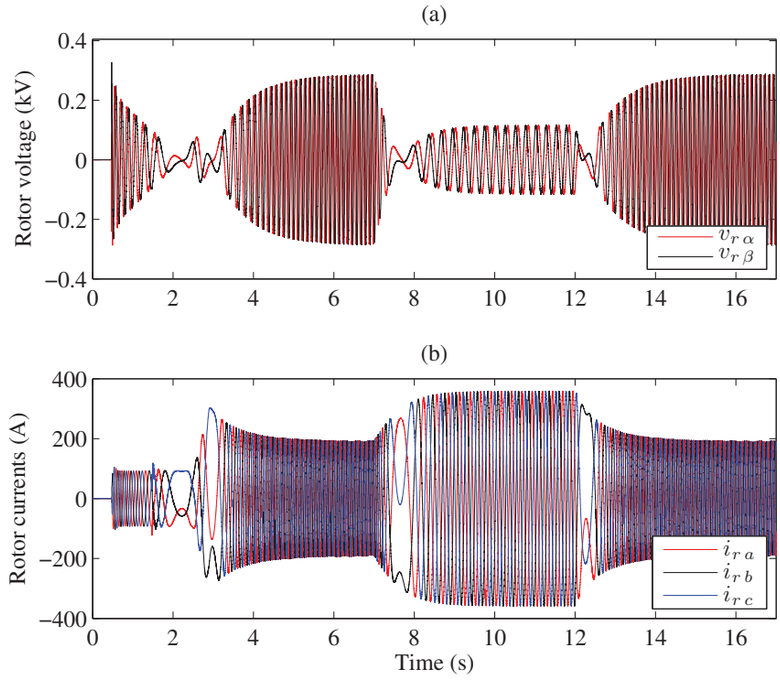

Fig. 12. Rotor voltage components fed into the SVM algorithm, and resulting three-phase rotor current

by the 1-SMC correspond to the gating signals of the RSC IGBTs, no additional modulation techniques —such as pulse-width modulation (PWM) or SVM— are required. In contrast, the

control signals produced by the proposed 2-SMC correspond to continuous voltage direct and quadrature components to be applied to the rotor by means of the RSC, which implies the use of intermediate SVM modulation. Furthermore, providing an additional procedure for bumpless transition between the algorithms devoted to synchronization and power control is indispensable for the case of the 2-SMC, but it is not required for the 1-SMC scheme.

Regarding parameter tuning, only the c constants included in the four switching functions considered need to be tuned for the case of the 1-SMC. It therefore turns out that satisfactory parameter adjustment is easily achieved by mere trial and error. However, in addition to those c constants, the λ and w gains present in the STAs must also be tuned for the 2-SMC variant. Even though, as stated in (Bartolini et al., 1999), it is actually the most common practice, trial and error tuning is not particularly effective in this latter case, as it may become highly time-consuming. Therefore, it is believed that there exists a strong need for development of alternative methods for STA-based 2-SMC tuning.

Concerning the switching frequency of the RSC IGBTs, it is fixed at 5 kHz in the case of the 2-SMC. On the contrary, it turns out to be variable, within the range from 0 to 20 kHz, for the 1-SMC algorithm. This feature complicates the design of both the back-to-back converter feeding the DFIG rotor and the grid-side AC filter, since broadband harmonics may be injected into the grid. As a result of the 25-μs sample time selected for the 1-SMC scheme, which leads to the aforementioned maximum switching frequency of 20 kHz, chatter observable in stator-side active and reactive powers is somewhat lower than $\pm$3% of the DFIG 660-kW rated power. Even a lower level of chatter arises from application of the SVM-based 2-SMC algorithm put forward. Furthermore, that chatter, or at least great part of it, is caused by the SVM, not by the 2-SMC algorithm itself.

Apart from the superior optimum power curve tracking achieved with both alternative SMC designs, the dynamic performance resulting from realization of the proposed 1-SMC scheme is noticeably better than that to which application of its 2-SMC counterpart leads. In effect, focusing on the state in which the DFIG stator is disconnected from the grid, HIL emulation results demonstrate that synchronization is reached faster by employing the 1-SMC algorithm. On the other hand, the power exchange between the DFIG and the grid taking place at the initial instants after connection is significantly lower when adopting the 1-SMC algorithm put forward, hence evidencing that its dynamic performance is also better for the stage during which power control is dealt with. The excellent dynamic performance reachable by means of its application supports the 1-SMC approach as a potential candidate for DFIG control under grid faults, where rapidity of response becomes crucial.

The main conclusions drawn from the comparison conducted in this section are summarized in Table 4.

	1-SMC ALGORITHM	2-SMC ALGORITHM
ALGORITHM COMPLEXITY	Relatively simple	More complex
PWM/SVM	Not required	Required
BUMPLESS PROCEDURE	Not required	Required
PARAMETER TUNING	Straightforward	Complex
SWITCHING FREQUENCY	Variable from 0 to 20 kHz	Fixed at 5 kHz
CHATTER LEVEL	$\pm$3% of the rated power	Lower
DYNAMIC PERFORMANCE	Excellent	Very good

Table 4. Comparison between the two SMC algorithms put forward

6. References

Abo-Khalil, A. G., Lee, D.-C. & Lee, S.-H. (2006). Grid connection of doubly fed induction generators in wind energy conversion system, *Proceedings of the CES/IEEE 5th International Power Electronics and Motion Control Conference (IPEMC 2006)*, Shanghai, China, vol. 3, pp. 1–5.

Arnaltes, S. & Rodríguez, J. L. (2002). Grid synchronisation of doubly fed induction generators using direct torque control, *Proceedings of the IEEE 28th Annual Conference of the Industrial Electronics Society (IECON 2002)*, Seville, Spain, pp. 3338–3343.

Åström, K. J. & Hägglund, T. (1995). *PID Controllers: Theory, Design and Tuning*, Instrument Society America, USA.

Bartolini, G., Ferrara, A., Levant, A. & Usai, E. (1999). On second order sliding mode controllers, *in* K. Young & Ü. Özgüner (eds), *Variable Structure Systems, Sliding Mode and Nonlinear Control*, Springer Verlag, London, UK, pp. 329–350.

Beltran, B., Ahmed-Ali, T. & Benbouzid, M. E. H. (2008). Sliding mode power control of variable-speed wind energy conversion systems, *IEEE Transactions on Energy Conversion* 23(2): 551–558.

Beltran, B., Ahmed-Ali, T. & Benbouzid, M. E. H. (2009). High-order sliding-mode control of variable-speed wind turbines, *IEEE Transactions on Industrial Electronics* 56(9): 3314–3321.

Beltran, B., Benbouzid, M. E. H. & Ahmed-Ali, T. (2009). High-order sliding mode control of a DFIG-based wind turbine for power maximization and grid fault tolerance, *Proceedings of the IEEE International Electric Machines and Drives Conference (IEMDC 2009)*, Miami, USA, pp. 183–189.

Ben Elghali, S. E., Benbouzid, M. E. H., Ahmed-Ali, T., Charpentier, J. F. & Mekri, F. (2008). High-order sliding mode control of DFIG-based marine current turbine, *Proceedings of the IEEE 34th Annual Conference of the Industrial Electronics Society (IECON 2008)*, Orlando, USA, pp. 1228–1233.

Blaabjerg, F., Teodorescu, R., Liserre, M. & Timbus, A. V. (2006). Overview of control and grid synchronization for distributed power generation systems, *IEEE Transactions on Industrial Electronics* 53(5): 1398–1409.

Ekanayake, J. B., Holdsworth, L., Wu, X. & Jenkins, N. (2003). Dynamic modeling of doubly fed induction generator wind turbines, *IEEE Transactions on Power Systems* 18(2): 803–809.

Kuo, B. C. (1992). *Digital Control Systems*, Oxford University Press, New York, USA.

Levant, A. (1993). Sliding order and sliding accuracy in sliding mode control, *International Journal of Control* 58(6): 1247–1263.

Ogata, K. (2001). *Modern Control Engineering*, Prentice Hall, Englewood Cliffs (New Jersey), USA.

Peña, R., Cárdenas, R., Proboste, J., Asher, G. & Clare, J. (2008). Sensorless control of doubly-fed induction generators using a rotor-current-based MRAS observer, *IEEE Transactions on Industrial Electronics* 55(1): 330–339.

Peña, R., Clare, J. C. & Asher, G. M. (1996). Doubly fed induction generator using back-to-back PWM converters and its application to variable-speed wind-energy generation, *IEE Proceedings - Electric Power Applications* 143(3): 231–241.

Peresada, S., Tilli, A. & Tonielli, A. (2004). Power control of a doubly fed induction machine via output feedback, *Control Engineering Practice* 12(1): 41–57.

Rashed, M., Dunnigan, M. W., MacConell, P. F. A., Stronach, A. F. & Williams, B. W. (2005). Sensorless second-order sliding-mode speed control of a voltage-fed induction-motor drive using nonlinear state feedback, *IEE Proceedings-Electric Power Applications* 152(5): 1127–1136.

Susperregui, A., Tapia, G., Zubia, I. & Ostolaza, J. X. (2010). Sliding-mode control of doubly-fed generator for optimum power curve tracking, *IET Electronics Letters* 46(2): 126–127.

Tapia, A., Tapia, G., Ostolaza, J. X. & Sáenz, J. R. (2003). Modeling and control of a wind turbine driven doubly fed induction generator, *IEEE Transactions on Energy Conversion* 12(2): 194–204.

Tapia, G., Santamaría, G., Telleria, M. & Susperregui, A. (2009). Methodology for smooth connection of doubly fed induction generators to the grid, *IEEE Transactions on Energy Conversion* 24(4): 959–971.

Tapia, G., Tapia, A. & Ostolaza, J. X. (2006). Two alternative modeling approaches for the evaluation of wind farm active and reactive power performances, *IEEE Transactions on Energy Conversion* 21(4): 901–920.

Utkin, V., Guldner, J. & Shi, J. (1999). *Siliding Mode Control in Electromechanical Systems*, Taylor & Francis, London, UK.

Utkin, V. I. (1993). Sliding mode control design principles and applications to electric drives, *IEEE Transactions on Industrial Electronics* 40(1): 23–36.

Vas, P. (1998). *Sensorless Vector and Direct Torque Control of AC Machines*, Oxford University Press, New York, USA.

Xu, L. & Cartwright, P. (2006). Direct active and reactive power control of DFIG for wind energy generation, *IEEE Transactions on Energy Conversion* 21(3): 750–758.

Yan, W., Hu, J., Utkin, V. & Xu, L. (2008). Sliding mode pulsewidth modulation, *IEEE Transactions on Power Electronics* 23(2): 619–626.

Yan, Z., Jin, C. & Utkin, V. I. (2000). Sensorless sliding-mode control of induction motors, *IEEE Transactions on Industrial Electronics* 47(6): 1286–1297.

Zhi, D. & Xu, L. (2007). Direct power control of DFIG with constant switching frequency and improved transient performance, *IEEE Transactions on Energy Conversion* 22(1): 110–118.

Sliding Mode Control

Edited by Prof. Andrzej Bartoszewicz

ISBN 978-953-307-162-6
Hard cover, 544 pages
Publisher InTech
Published online 11, April, 2011
Published in print edition April, 2011

The main objective of this monograph is to present a broad range of well worked out, recent application studies as well as theoretical contributions in the field of sliding mode control system analysis and design. The contributions presented here include new theoretical developments as well as successful applications of variable structure controllers primarily in the field of power electronics, electric drives and motion steering systems. They enrich the current state of the art, and motivate and encourage new ideas and solutions in the sliding mode control area.

InTech Europe
University Campus STeP Ri
Slavka Krautzeka 83/A
51000 Rijeka, Croatia
Phone: +385 (51) 770 447
Fax: +385 (51) 686 166
www.intechopen.com

InTech China
Unit 405, Office Block, Hotel Equatorial Shanghai
No.65, Yan An Road (West), Shanghai, 200040, China
中国上海市延安西路65号上海国际贵都大饭店办公楼405单元
Phone: +86-21-62489820
Fax: +86-21-62489821

IntechOpen